

# Cross-Plane Carrier Transport in Van der Waals Layered Materials

Sina Najmaei,\* Mahesh R. Neupane, Barbara M. Nichols, Robert A. Burke, Alexander L. Mazzone, Matthew L. Chin, Daniel A. Rhodes, Luis Balicas, Aaron D. Franklin, and Madan Dubey\*

The mechanisms of carrier transport in the cross-plane crystal orientation of transition metal dichalcogenides are examined. The study of in-plane electronic properties of these van der Waals compounds has been the main research focus in recent years. However, the distinctive physical anisotropies, short-channel physics, and tunability of cross layer interactions can make the study of their electronic properties along the out-of-plane crystal orientation valuable. Here, the out-of-plane carrier transport mechanisms in niobium diselenide and hafnium disulfide are explored as two broadly different representative materials. Temperature-dependent current–voltage measurements are performed to examine the mechanisms involved. First principles simulations and a tunneling model are used to understand these results and quantify the barrier height and hopping distance properties. Using Raman spectroscopy, the thermal response of the chemical bonds is directly explored and the insight into the van der Waals gap properties is acquired. These results indicate that the distinct cross-plane carrier transport characteristics of the two materials are a result of material thermal properties and thermally mediated transport of carriers through the van der Waals gaps. Exploring the cross-plane electron transport, the exciting physics involved is unraveled and potential new avenues for the electronic applications of van der Waals layers are inspired.

## 1. Introduction

The study of carrier transport in transition metal dichalcogenides (TMDs) has primarily focused on planar crystal orientations.<sup>[1]</sup> Yet, the remarkable characteristics of the crystal

Dr. S. Najmaei, Dr. M. R. Neupane, Dr. B. M. Nichols, Dr. R. A. Burke, A. L. Mazzone, M. L. Chin, Dr. M. Dubey  
Sensors and Electron Devices Directorate  
United States Army Research Laboratory  
2800 Powder Mill Road, Adelphi, MD 20783, USA  
E-mail: sina.najmaei.civ@mail.mil; madan.dubey.civ@mail.mil

Dr. R. A. Burke  
General Technical Services, LLC  
1451 Route 34 South—Suite 301, Wall Township, NJ 07727, USA

Dr. D. A. Rhodes, Prof. L. Balicas  
National High Magnetic Field Laboratory  
Florida State University  
1800 E. Paul Dirac Drive, Tallahassee, FL 32310, USA

Prof. A. D. Franklin  
Department of Electrical and Computer Engineering  
Duke University  
Durham, NC 27708, USA

DOI: 10.1002/sml.201703808

cross-plane (out-of-plane) orientation in layered materials and the weak layer–layer interactions define many of their less explored, unique physical properties and striking anisotropies.<sup>[2]</sup> This is clearly illustrated in the unconventional cross-plane electronics of layered materials such as graphite.<sup>[2c,3]</sup> The cumulative effects of 2D layer properties that delocalize or extend electron cloud densities in the neighboring planes and the physical separation defined by the interplane potential barriers can result in cross-plane electronic transport unique to layered systems.<sup>[2c,3]</sup> Hence, understanding the governing mechanism and the role of the van der Waals gap (vdWg) in the cross-plane carrier transport within multilayered materials is essential to expand their applicability into novel application domains.

The study of graphite's electronic anisotropy has led to the development of models that try to explain the origins of the significant differences in the material's planar and cross-plane electrical conductivities.<sup>[2c]</sup> It has been shown that by using a band-like model for graphite, the mechanism involved can be explained using the differences in the carrier masses along the different crystal orientations.<sup>[2c]</sup> Alternatively, using a more descriptive model for the layered crystal structure, these effects are attributed to the nature of cross-plane conduction, and the field- and thermally assisted hopping of carriers between the layers.<sup>[2c,d]</sup> These studies, involving relatively thick crystals of graphite, were later followed by experiments on intercalated compounds that support the notion that the van der Waals gap and interlayer interaction between the layers play a central role in the cross-plane electron transport.<sup>[4]</sup> In recent years, utilizing the weak interlayer interactions in layered materials and the unprecedented access to extreme 2D-confined physical regimes have uncovered many more exciting cross-plane properties, such as thermoelectric effects and field-effect tunneling.<sup>[5]</sup> However, the research examining and utilizing the anisotropy in the thermal and electrical conductivities of the confined layers lacks a fundamental understanding of the underlying mechanisms involved.

In this paper, we examine the cross-plane carrier transport properties of layered transition metal dichalcogenides. We

explore the interlayer conductivity properties of niobium diselenide ( $\text{NbSe}_2$ ) and hafnium disulfide ( $\text{HfS}_2$ ) with very distinct planar characteristics. The temperature dependency of the electronic transport reveals a contrasting behavior in the two materials because of their distinct structural and electronic properties. Using tunneling models and first principles calculations, we examine and quantify these differences. We use these findings to propose and test a basic model that explains the cross-plane electron transport properties in van der Waals (vdW) layered compounds through trap-based and hopping conduction. Raman spectroscopy reveals the thermal response of the bonds and structural properties of the materials. The results indicate that the vdWg and the changes in potential barriers between the layers dominate the transport of carriers in the cross-plane orientation.

## 2. Results and Discussions

Many of the electronic and transport properties of TMDs are defined by the s- and the p-orbitals of the chalcogen atoms (S, Se, Te, etc.) contributing to the valence band, the transition

metal's (Mo, W, Nb, Hf, etc.) d-orbitals forming the conduction band, and the magnitude of the charge transfer between the metal–ligands.<sup>[6]</sup> Similarly, the distinct metallic and semi-conducting behaviors of  $\text{NbSe}_2$  and  $\text{HfS}_2$ , respectively, are partly due to the bonding configuration and the resultant band structure of these materials. The half-filled Nb 4d-orbitals in  $\text{NbSe}_2$  are responsible for its planar metallic state.<sup>[6c]</sup> In contrast, the empty Hf 5d-orbitals in  $\text{HfS}_2$  create a planar insulating behavior, with an indirect bandgap ( $E_g \approx 2.0$  eV) in bulk.<sup>[7]</sup> These TMDs can also be distinguished by their structural arrangements. Two structural stacking polytypes, 1T and 2H, are most commonly observed in these layered materials (Figure 1a).  $\text{NbSe}_2$  displays the 2H stacking order while  $\text{HfS}_2$  is most stable in its 1T configuration. The stacking arrangement of the atoms and the weak interlayer interactions between the ligands in the form of van der Waals forces create empty spaces between the layers in both materials (i.e., vdWg) (Figure 1a). The planar and interlayer electronic and transport properties of TMDs are highly influenced by the magnitude of vdWg. A recent comprehensive study on multilayered  $\text{MoS}_2$ , involving

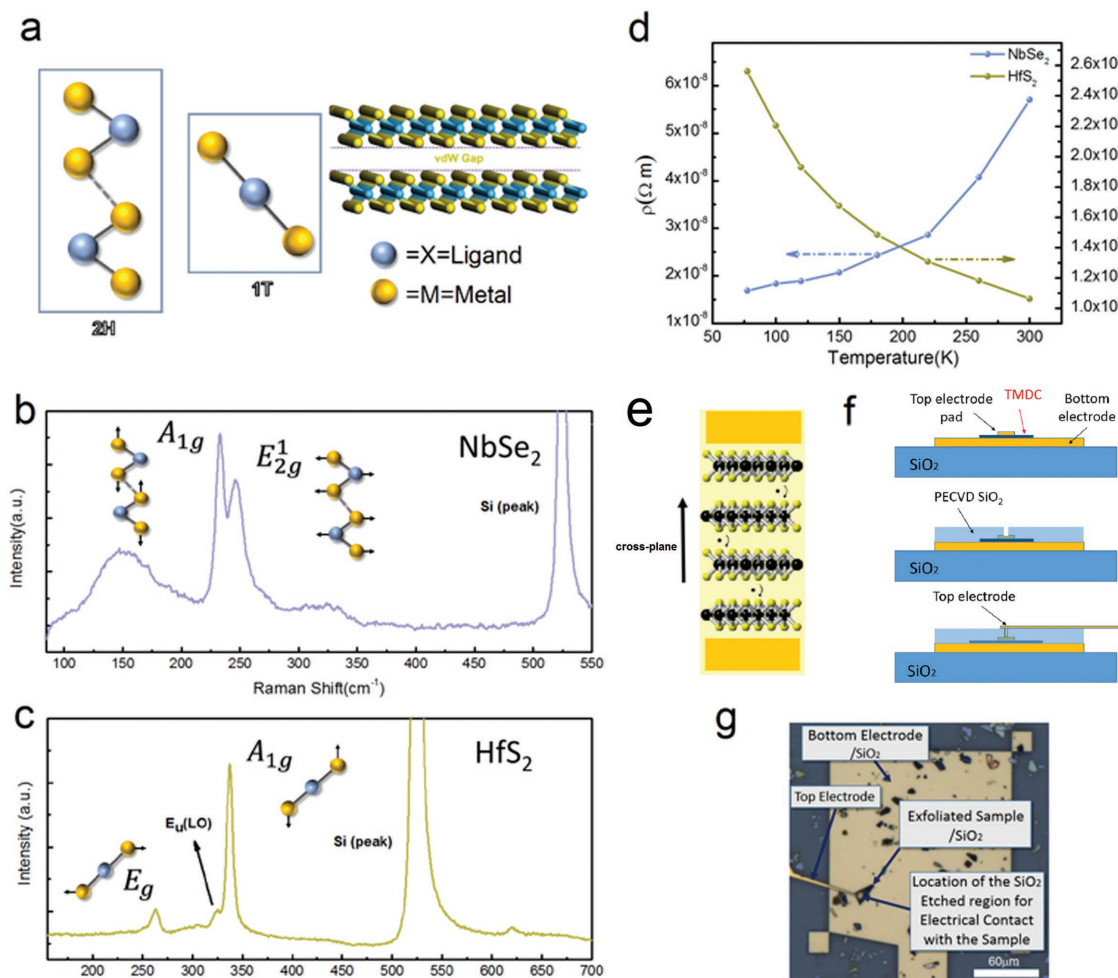


**Figure 1.** Basic chemical and structural characterization of  $\text{NbSe}_2$  and  $\text{HfS}_2$  samples. a) Structural characteristics of both compounds. Raman spectra acquired for b)  $\text{NbSe}_2$  and c)  $\text{HfS}_2$  at 100 K. The insets show vibrational modes in both materials next to the respective peaks. d) Temperature-dependent resistivity of  $\text{NbSe}_2$  and  $\text{HfS}_2$ . e) Device configuration for electrical transport measurements along the cross-plane. f) Fabrication steps for preparing the devices. g) Top-view optical image of a device.

both theory and experiment, suggests that the magnitude of vdWg could, in fact, transform a multilayered 2D material with indirect bandgap to a direct bandgap, behaving like a single layer 2D material.<sup>[8]</sup> However, the effect of the vdWg on the overall transport properties of these layered materials such as NbSe<sub>2</sub> and HfS<sub>2</sub> is still unknown.

It is known that the vdWg plays an important role in the TMD properties such as the band structure, the molecular bonds, and the molecular vibrations.<sup>[9]</sup> The nonionic interlayer interactions due to the vdWg between the layers in TMDs can be described by the attractive van der Waals and short-range repulsive, and long-range coulombic forces between the layers. The charge transfer between the ligand and the metal atoms of the TMDs creates the long-range interlayer coulombic interaction. Hence, the strength of these interactions and their dependence on the magnitude of the charge transferred between the chalcogen and the transition metal component is a distinguishing feature of the vdWgs among the different TMDs.<sup>[10]</sup> For carrier transport along the cross-plane, the charge carriers have to screen through the potential barriers created by the interlayer vdWg, and hence, the quality and magnitude of the vdWg play a prominent role on the overall transport properties. Chemical bonds in NbSe<sub>2</sub> result in a highly delocalized free electron cloud and hence are metallic in nature. In contrast, the transfer of charges from the metal atoms to the ligands in HfS<sub>2</sub> (one of the highest transfer rates among the transition metal dichalcogenide family with a localized effective charge of  $e_1 \approx 2.6e$ ) results in a strong ionicity of its bonds.<sup>[10]</sup> As a result, the long-range coulombic interactions and the balancing forces that define the vdWg properties in NbSe<sub>2</sub> and HfS<sub>2</sub> are vastly different in nature. Therefore, we expect that the study of their cross-plane carrier transport properties will shine light on the underlying mechanisms involved.

To examine the cross-plane electron transport in transition metal dichalcogenides, we prepared bulk samples of NbSe<sub>2</sub> and HfS<sub>2</sub> using the chemical vapor transport technique (see the “Experimental Section” for details). Single crystals were then mechanically exfoliated onto SiO<sub>2</sub>/Si substrates that were patterned with gold electrodes. Using this process, we were able to prepare samples of varying thicknesses for their characterization and subsequent device fabrication. Once the exfoliation was complete, Raman spectroscopy was utilized to obtain valuable information about the structural and electronic properties of the TMDs. Raman spectra acquired from our exfoliated samples confirm the presence of 2H-NbSe<sub>2</sub> and 1T-HfS<sub>2</sub> (Figure 1b,c). 2H-NbSe<sub>2</sub> belongs to the  $D_{6h}^4$  space group and has 18 normal vibrational modes at the Brillouin zone center. It has been shown that the dynamic nature of the NbSe<sub>2</sub> Raman peaks closely follow the electronic transitions from an undistorted metallic phase at room temperature to an incommensurate charge-density wave phase transition below 33 K.<sup>[11]</sup> For NbSe<sub>2</sub>, we observe the Raman active modes  $E_{2g}^1$  at  $\approx 246$  cm<sup>-1</sup> and  $A_{1g}$  at  $\approx 233$  cm<sup>-1</sup>. Generally, the separation between the in-plane and out-of-plane vibrational modes in the Raman spectra, when compared to other TMDs such as MoS<sub>2</sub>, is indicative of near isotropy in the ligand–metal and ligand–ligand bond strengths.<sup>[12]</sup> This is believed to be due to the metallic nature of the bonds in this material. The broad peak centered at  $\approx 153$  cm<sup>-1</sup> (linewidth = 65 cm<sup>-1</sup>) has been attributed

to scattering by two longitudinal acoustic phonons on the  $\Sigma$  branch from opposite sides of the Brillouin zone (BZ).<sup>[11]</sup>

The  $D_{3d}^3$  space group symmetry of 1T-HfS<sub>2</sub> originates from two Raman active modes ( $A_{1g}$  and  $E_g$ ) and four infrared active modes ( $2A_{2u}$  and  $2E_u$ ). In the Raman spectra acquired from the HfS<sub>2</sub> samples, we observe the  $E_g$  ( $\approx 262$  cm<sup>-1</sup>),  $A_{1g}$  ( $\approx 338$  cm<sup>-1</sup>), and  $E_u$  longitudinal optical (LO) ( $\approx 325$  cm<sup>-1</sup>) modes.<sup>[13]</sup> In addition, we observe a weak, broad peak located between 600 and 700 cm<sup>-1</sup>, which is indicative of a weak second-order effect.<sup>[13b]</sup> The excitation energy at 2.33 eV is significantly off resonance with respect to the direct optical transitions at the  $\Gamma$ -point of HfS<sub>2</sub>; therefore, a better resolution of the individual peaks contained here is not possible.<sup>[13b]</sup> The X-ray photoelectron spectra acquired from these crystals and presented in Figure S1 of the Supporting Information confirm the bonding characteristics of NbSe<sub>2</sub> and HfS<sub>2</sub>.

Further understanding of the electronic structure of the materials can be achieved through electrical transport measurements. For this, we fabricated planar devices on both materials and characterized their transport properties. Using atomic force microscopy, we estimate the thickness of the flakes chosen for the measurements as roughly 30 nm for both NbSe<sub>2</sub> and HfS<sub>2</sub>. The magnitude of the resistivity for NbSe<sub>2</sub> samples and the temperature dependence presented in Figure 1d indicate a metallic planar conductivity. The temperature coefficient  $\alpha$  for NbSe<sub>2</sub> is estimated to be  $\approx 0.0053$  K<sup>-1</sup> ( $\alpha = \frac{1}{R_0} \frac{dR}{dT}$  where  $R$ ,  $R_0$ , and  $T$  are the resistance, the resistance at a reference temperature, and the temperature, respectively). In contrast, the temperature dependence of the planar resistivity in HfS<sub>2</sub> samples shows a highly insulating behavior with a temperature coefficient of  $\approx -0.0038$  K<sup>-1</sup> (Figure 1d).

To study the cross-plane electron transport in these materials, we prepared devices with cross-sectional diameters of 1  $\mu$ m and vertical configuration presented in Figure 1e. The NbSe<sub>2</sub> and HfS<sub>2</sub> samples varied in thickness ranging from 8 to 130 nm and had a minimum cross-sectional diameter of 1  $\mu$ m. To prepare these devices, we used multiple lithography, metal and oxide deposition, and oxide etching steps (Figure 1f). After the flakes are placed on the bottom electrodes, they are covered with plasma-enhanced chemical vapor deposition (PECVD) grown SiO<sub>2</sub> and accessed via an etch step to prepare the top electrode (further details on the device fabrication is provided in the “Experimental Section”). The optical image of a completed device, illustrating its general design, is shown in Figure 1g. Test devices that allowed evaluation of the fabrication process were also prepared. In these test devices, we examined the electrically shorted behavior by making direct contact to the bottom electrode. Our results indicate a good electrical contact and confirm a complete SiO<sub>2</sub> etch step. Additionally, by omitting the etch step in some of the test structures, we were able to evaluate the leakage current through the PECVD–SiO<sub>2</sub> layer, which shows no significant leakage up to driving voltages in the order of 40 V.

We next examined the thickness dependence of the cross-plane carrier transport through the vdWgs in our devices and their current–voltage characteristics. Thickness variation leads to the change in the number of vdWgs that charge carriers need to overcome, and allows for a direct and systematic probe

of the vdWg's role in the cross-plane transport of TMD materials. It has been shown that at higher fields the movement of ions and defects can contribute to the transport of carriers and modify the current–voltage characteristics.<sup>[14]</sup> In our measurements we observe a significant onset of hysteresis in the  $I$ – $V$  characteristics of the devices at high fields ( $\approx 0.5$  V) (Figure S2, Supporting Information). Hence, in our experiments we set a maximum applied bias voltage of 0.2 V to prevent these effects from influencing our results. Further experiments are needed to understand the high-field behavior of the cross-plane transport in these materials. The results of the current–voltage measurements for NbSe<sub>2</sub> and HfS<sub>2</sub> devices of varied thickness are summarized in **Figure 2**. As the results clearly indicate, NbSe<sub>2</sub> and HfS<sub>2</sub> cross-plane conductivity behavior shows an anomalous behavior with respect to bulk non-vdW materials and, when compared to each other, there are glaring differences in the carrier transport properties of the two material systems. For the case of NbSe<sub>2</sub>, because of its metallic nature, the device conductivity is higher than HfS<sub>2</sub> and shows moderate channel length dependence (Figure 2a). In contrast HfS<sub>2</sub> device conductivity shows a strong channel length dependence (five orders of magnitude over the studied thickness range) (Figure 2a). For thin samples, the differences between the cross-plane current densities of HfS<sub>2</sub> and NbSe<sub>2</sub> devices essentially approach similar magnitudes. However, a key dissimilarity in the behavior of the two materials is the opposing channel length dependence trends seen in NbSe<sub>2</sub> and HfS<sub>2</sub> devices. These channel dependencies also suggest that the cross-plane electron transport is predominantly effected by the material properties rather than the contact and interface properties. Hence, a more complete picture of the material behavior is exposed through

the combined effects of thickness and temperature on the cross-plane transport as summarized in Figure 2b,c. For thin ( $<10$  nm) NbSe<sub>2</sub> samples, the conductivities decrease as the temperature increases (Figure 2b). For thicker NbSe<sub>2</sub> samples, a gradual change in the temperature dependence is observed. The change at lower temperatures begins with a sharp increase in conductivity, followed by a plateau region for medium range temperatures and a steady decrease in conductivity at elevated temperatures. Overall, the HfS<sub>2</sub> conductivities show a stronger and uniform temperature dependence with five orders of magnitude change in the examined temperature range (Figure 2c). The conductivities in thicker samples show more sensitivity to changes in temperature. Additionally, the changes in cross-sectional area of our devices show little effect on the conductivity of the devices in the diameter ranges measured (0.5–2  $\mu$ m) (Figure S3, Supporting Information).

Our results can be summarized and displayed by calculating the temperature coefficient. The map of the temperature coefficient as a function of both layer thickness and temperature is shown in Figure 2d,e. The magnitudes and thickness dependence of the temperature coefficients reflects on the greater temperature dependence of the cross-plane carrier transport. In NbSe<sub>2</sub> samples, an anomalous behavior is clearly visible where a transition from a positive to negative temperature coefficient is observed as outlined by the dashed line (**Figure 3d**). The negative values in the HfS<sub>2</sub> samples are similar to the behavior expected of a semiconductor; however, the very high magnitudes for temperature coefficient,  $\alpha \approx 0.05$  K<sup>-1</sup>, reaching one order of magnitude larger than the planar values, is intriguing. In addition the anisotropy ratios ( $\rho_c/\rho_a$ ) for the  $c$ -axis versus basal plane resistivity of the materials provides further insight

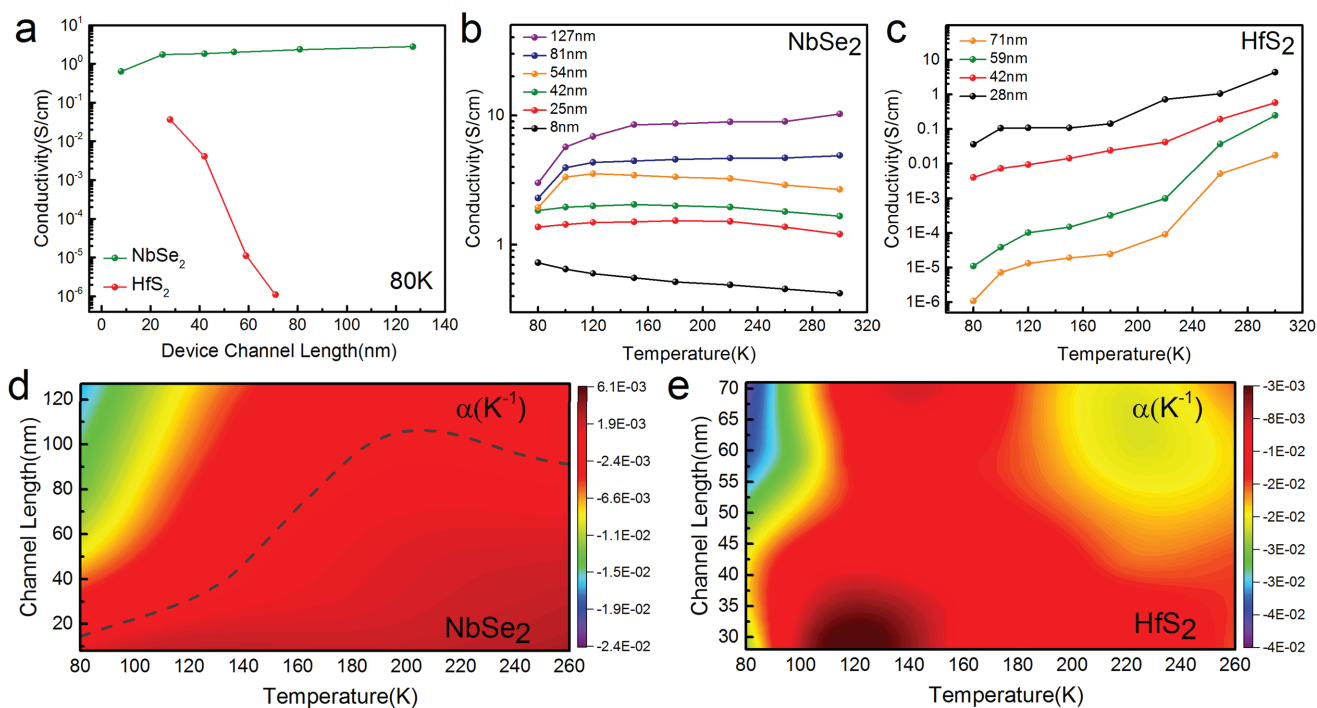


**Figure 2.** Cross-plane electron transport measurements a) the thickness-dependent conductivity for NbSe<sub>2</sub> and HfS<sub>2</sub> samples measured at 80 K. Temperature-dependent conductivity of b) NbSe<sub>2</sub> and of c) HfS<sub>2</sub> samples under 0.2 V of applied bias voltage. The map of the temperature coefficient as a function of the layer thickness and of the temperature for d) NbSe<sub>2</sub> and e) HfS<sub>2</sub> samples.

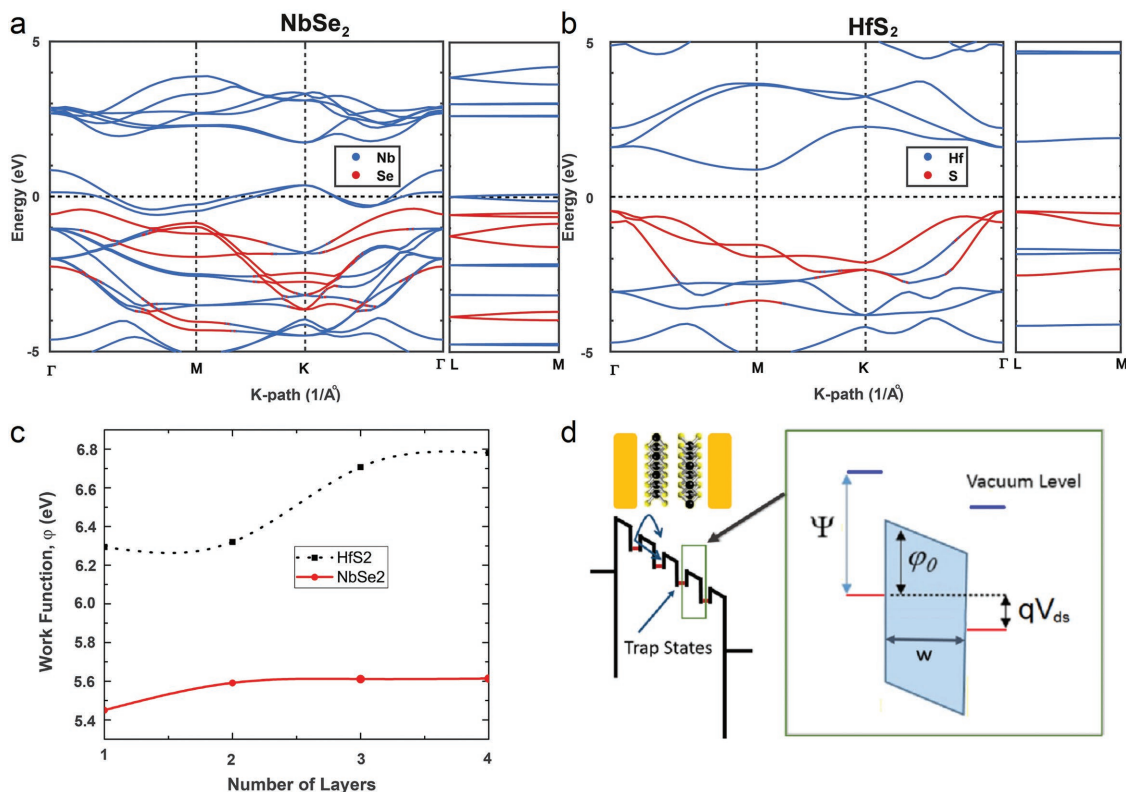


**Figure 3.** First principles calculations and tunneling model. The band structures of bulk a) NbSe<sub>2</sub> and b) HfS<sub>2</sub> calculated from the first principles calculations. c) Calculated work functions for NbSe<sub>2</sub> and HfS<sub>2</sub> as a function of the number of layers. d) Tunneling model for layered materials describing the van der Waals gaps as barriers and the atomic layers as localized charge trap states.

into the distinctions between the two material systems and the mechanisms of transport. For similar material thicknesses at room temperature, the NbSe<sub>2</sub> anisotropy is in the order of 10<sup>5</sup> while in HfS<sub>2</sub> it is roughly 10<sup>-6</sup>. The anisotropy ratios and the temperature dependence of the cross-plane conductivity in NbSe<sub>2</sub> are similar to what have been measured for graphite. However HfS<sub>2</sub> behaves very differently and the cross-plane conductivity is six orders of magnitude higher than its planar conductivity.

To explain these observations, we can resort to band theory for the cross-plane transport. These models can, to some extent, explain the anisotropy ratios in bulk graphite by comparing the carrier masses in different crystal orientations. However, it has been shown that they are incompetent in capturing the temperature dependence effects and the wide range of experimental results.<sup>[3-7]</sup> Our results, expanding the cross-plane measurements into a wider range of layered materials and thicknesses, show similar deficiencies. The band structure of NbSe<sub>2</sub> and HfS<sub>2</sub> presented in Figure 3a,b demonstrates the dispersion of the conduction band close to multiple symmetry points. The hybrid functional corrected energy gap for the bulk HfS<sub>2</sub> is ≈2.1 eV, which is consistent with earlier reported experimental and theoretical values.<sup>[7]</sup> The valence and conduction bands of HfS<sub>2</sub> are mainly composed contributions from Hf and S atoms, respectively. The results show that in both NbSe<sub>2</sub> and HfS<sub>2</sub> the bands from L to M (out-of-plane direction) are distinctively flat while significantly more dispersive in the other in-plane

directions. This is a common characteristic of 2D materials with weak vdW forces between the layers. The  $m^*$  is inversely correlated with the carrier mobility and, in general, is evaluated by fitting the band edges to a parabola according to  $E(k) = \frac{-\hbar^2 k^2}{2m_0 m^*}$ , where  $m_0$  is the rest mass.<sup>[15]</sup> In addition, the  $m^*$  is also characterized by the curvature of the bands around the band edges in momentum space. Though an accurate theoretical calculation of carrier effective mass using density functional theory (DFT) requires an inclusion of spin-orbit coupling (SOC) and the denser grid points in the k-point mesh,<sup>[15,16]</sup> an analysis of the band dispersion around edges gives a qualitative measure of the effective mass. Hence, a simple visual inspection of the curvatures of the bands highlights a qualitative difference between the mobilities in the in-plane and out-of-plane directions of both compounds. This is consistent with the estimated out-of-plane effective mass for the bulk HfS<sub>2</sub>, which is roughly 15 times larger than its in-plane values.<sup>[17]</sup> This anisotropy in carrier masses and the corresponding conductivity along the different crystal orientations of the 2D materials predict the anisotropy ratios ( $\rho_c/\rho_a$ ) for both materials. In NbSe<sub>2</sub>, this analysis can provide some insight into the transport properties but does not provide a comprehensive understanding of the cross-plane transport in the material and certainly lacks the ability to explain our observations for HfS<sub>2</sub>. Clearly the cross-plane carrier transport within layered materials is highly influenced by the scattering of carriers across the vdWgs. A systematic study correlating the

number of vdWgs and effective masses (mobilities) might further elucidate this behavior, which is planned for a future study. However, the assumption of perfect periodicity and application of Bloch theory to calculate the band structure of the material in the extremely thin cross-plane orientation may not be precise.<sup>[18]</sup> Conceivably, in order to interpret our results, a different material model may be necessary for accurate determination of the electronic transport along the cross-plane orientation. Thus, we propose and examine the suitability of a thermally activated process involving the transport of carriers through barriers imposed by the vdWgs in the layered structure.

To understand the mechanisms involved in the cross-plane carrier transport in layered materials, we developed a model based on the tunneling transport of carriers through the layers (Figure 3d). This process entails several mechanisms. For the carriers to conduct, they need to be injected into the channel followed by tunneling through the layers overcoming the potential barriers imposed by vdWgs. The carriers in layered materials are confined by the vdWgs along the cross-plane and are only free to move within the planar orientation which makes them practically localized within the layers. Therefore, we treat the layers as a series of trap states separated by barriers that represent the vdWgs (Figure 3d). In this model, the carriers need to be emitted from the metals into the free space, i.e., vdWg, and move into the trap states. They can also directly tunnel between the metallic contacts or escape from the traps and contribute to the current. The barrier potential for charge injection to the layers from the metallic contacts can be estimated using the Schottky–Mott approximation and is associated with the relative work function of the materials. The estimated layer-dependent work functions for intrinsic NbSe<sub>2</sub> and HfS<sub>2</sub>, using first principles DFT calculations, are shown in Figure 3c. From the thickness-dependent trends, one can infer that for the samples examined in this study (more than four layers), the work function values converge to their bulk values. Therefore, Schottky–Mott barrier heights experienced by electrons moving from the gold metal contacts with a work function of ≈5.1 eV, as predicted by the DFT calculation, to the first layer of the materials in our devices are quantitatively independent of thickness. Consequently, the metal–semiconductor barrier in its entirety might not be responsible for the devices' current–voltage dependencies on thickness and temperature as shown in Figure 2. Therefore, a focus on describing the transport of carriers in the bulk of the channel, i.e., between the individual layers of NbSe<sub>2</sub> and HfS<sub>2</sub>, should be adequate to describe the cross-plane transport. We employed three mechanisms of tunneling,  $J_{D-T}$ , the direct or field tunneling,  $J_{P-F}$ , Poole–Frenkel trap-based tunneling, and  $J_{H-C}$ , hopping conduction through the layers to describe all possible mechanisms of current conduction.<sup>[19]</sup> The total current density is defined as the sum of the currents densities describing the above mentioned tunneling mechanisms, and is given by the following relation:

$$J = J_{D-T}(F) + J_{P-F}(T, F, D) + J_{H-C}(T, F, s) \quad (1)$$

Here, the direct tunneling is dependent on the applied field; the trap-based tunneling is dependent on the applied field, temperature, and trap density of states; and the hopping conduction is dependent on the applied field, temperature, and

hopping distance. The individual tunneling mechanisms can be described using the relationships described here<sup>[19]</sup>

$$J_{D-T} \propto F^2 \exp\left[-\frac{C}{E} \phi_b^{-3}\right] \quad (2)$$

$$J_{P-F} \propto D V \exp\left[\frac{q}{kT} (a\sqrt{V} - \phi_b)\right] \quad (3)$$

$$J_{H-C} \propto \exp\left[\frac{1}{kT} (qsF - \phi_b)\right] \quad (4)$$

where  $C$  and  $a$  are constants,  $F = \frac{V}{d}$  is the applied field,  $V$  is the applied voltage,  $d$  is the channel thickness,  $k$  is the Boltzmann constant,  $D$  is the density of states,  $q$  is the electronic charge,  $s$  is the average space between the traps, and  $\phi_b$  is the barrier height.<sup>[19c]</sup> The direct field tunneling between the metals is highly sensitive to the barrier width. Therefore, this mechanism is only a significant contributor to the current in thin samples. The trap-based P-F tunneling and hopping conduction are thermally mediated processes and describe the tunneling of carriers in the bulk of the channel between the trap states. The P-F mechanism describes tunneling processes that involve the thermal emission of carriers from the traps, while the hopping mechanism describes the direct tunneling between them. Hence, P-F tunneling is more influential at high temperatures while the hopping mechanism governs the low-temperature and high-electric-field regimes. Thermal energy reshuffles the electrons in the energies and controls the statistics of empty and occupied states in the hopping transport, but its strong field dependence makes it more significant at higher fields.

A quantitative application of the barrier models can shine light on the characteristics of the cross-plane transport. This can be accomplished by looking at the plots of  $\ln(I/V)$  versus  $1/T$  and  $\sqrt{V}$  to examine the trap-based tunneling effects. We looked at the current–voltage characteristics and the temperature dependence of the carrier transport in the devices that were made on exfoliated samples. Figure 4a,b for the NbSe<sub>2</sub> devices and Figure 4c,d for HfS<sub>2</sub> devices made of flakes with similar thicknesses (roughly 40 nm thick), display the measured current–voltage characteristics as a function of the inverse temperature and of the square root of the voltage, respectively. This representation will allow us to use the appropriate fitting models to examine the interlayer transport. Nevertheless, these results demonstrate that the HfS<sub>2</sub> samples show a strong, and well-behaved, thermally activated dependence on temperature, while the behavior of the NbSe<sub>2</sub> requires more attention. A thermally activated process dominates the temperature dependence of both NbSe<sub>2</sub> and HfS<sub>2</sub> samples. The HfS<sub>2</sub> samples follow a regular Poole–Frenkel plot ( $J$ – $V$  based on relationship (3)) with two distinct regimes of transport that is activated at a temperature close to 160 K. We hypothesize that at temperatures above 160 K, the trap-based tunneling is the main mechanism involved. By fitting the linear portion of this region, we can estimate the average barrier height for trap-based tunneling in HfS<sub>2</sub>. In NbSe<sub>2</sub> devices, at temperatures above 120 K, an irregular Poole–Frenkel behavior emerges that needs further consideration. Based on evidence suggesting that the barrier height

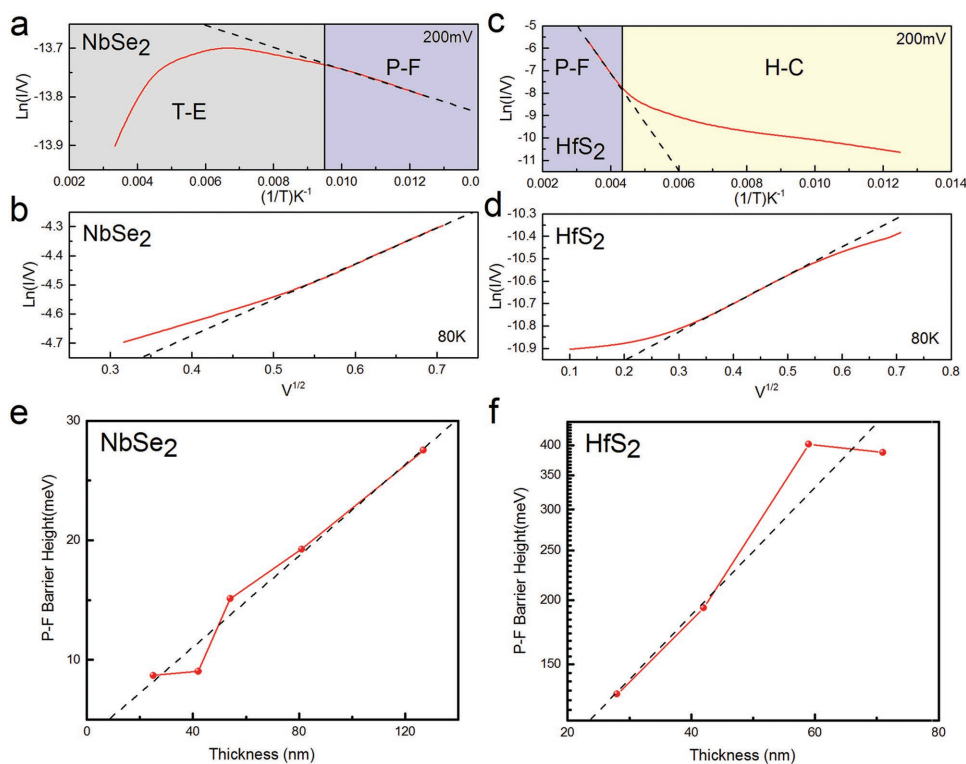


**Figure 4.** The Poole–Frenkel tunneling in NbSe<sub>2</sub> and HfS<sub>2</sub> samples. The Poole–Frenkel current density plots for NbSe<sub>2</sub> a) temperature and b) field dependence. The Poole–Frenkel current density plots for HfS<sub>2</sub> c) temperature and d) field dependence. The results are color-coded to distinguish between the dominance of different mechanisms on transport at the specified temperature regimes. Pool–Frenkel is annotated by P-F, a region of dominance for thermal expansion effects is marked as T-E, and the hopping conduction is represented by H-C. The thicknesses of the NbSe<sub>2</sub> and HfS<sub>2</sub> samples are ≈40 nm. The estimated Poole–Frenkel barrier height as a function of sample thickness for e) NbSe<sub>2</sub> and f) HfS<sub>2</sub> samples.

in NbSe<sub>2</sub> is significantly smaller when compared to HfS<sub>2</sub>, the thermally activated trap-based transport can be considered to be the leading mechanism in the temperature range of 80–120 K for this material. Therefore, we can estimate the average barrier height of the NbSe<sub>2</sub> devices using the linear portion of the plots. We plot the estimated barrier heights for NbSe<sub>2</sub> and HfS<sub>2</sub> samples as a function of thickness in Figure 4e,f.

The estimated barrier heights represent the average energy required by the trapped carriers to escape. The barrier height in HfS<sub>2</sub> is roughly one order of magnitude larger than in NbSe<sub>2</sub> (Figure 4e,f). This is likely due to differences in the lowest unoccupied molecular orbital levels in the two materials, their vdWg properties, and the level of charge localization within the layers. The delocalized carriers in NbSe<sub>2</sub> layers, owing to its metallic bonds, contribute to the lower barrier heights in this material. In contrast, the strongly localized charge in HfS<sub>2</sub> bonds is responsible for their larger barrier heights. Concomitantly, ignoring metal–semiconductor interactions, the energy difference between the work functions for the four-layered systems, as shown in Figure 3c, and the metal (Au) work function gives a quantitative difference in the barrier heights of ≈1 eV between NbSe<sub>2</sub> and HfS<sub>2</sub>. The gradual increase in the barrier height with respect to thickness may be a result of the models' inability to describe the transport behavior for every thickness regime. For instance, in thin samples, direct tunneling and defect-mediated conduction mechanisms can play a more significant role and can limit the efficacy of the model in describing the

current–voltage characteristics. At lower temperatures, carrier hopping is considered to be the dominant source of conduction. For the HfS<sub>2</sub> samples, we can plot  $\ln(J)$  versus  $1/T$  and  $F$  to explore the hopping conduction model (Figure 5a,b). The estimated barrier height for hopping conduction in HfS<sub>2</sub> as a function of the thickness is shown in Figure 5c. The estimated hopping distance for the devices with respect to thickness has been presented in Figure 5d. The average hopping distance in these devices is roughly 2.2 nm which is equivalent to ≈3 layers of HfS<sub>2</sub>. Our results exemplify the importance of barrier properties and demonstrate how the characteristics of the vdWgs, such as width and energetics, can control the cross-plane carrier conduction. It is important to note that in this analysis we have not considered the role of material defects. While more elaborate experimentations are needed to decipher the role of material imperfections, stating the limitations they impose is essential to accurate inferences from the results. Defects lead to midgap states that are typically deep in transition metal dichalcogenides.<sup>[20]</sup> Defect states in the layers, therefore, could be modeled similar to the traps defined for the cross-plane transport of free electrons with tentatively higher barrier heights. Therefore, the presence and changes in the densities of these defects should result in changes in the average estimates for barrier height and hopping distance. However, as our samples are prepared from the same bulk crystal, we anticipate a uniform density of defects in our devices and presume that the general conclusions about the thickness and temperature

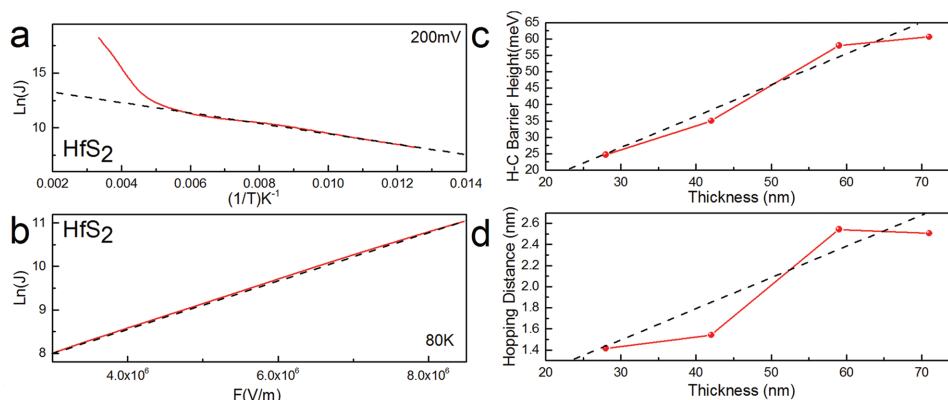


**Figure 5.** Hopping conduction model for the low-temperature regime cross-plane carrier transport in HfS<sub>2</sub>. The plot of HfS<sub>2</sub> current densities versus a) temperature and b) electric field for estimation of hopping conduction constants in high electric field and low-temperature regimes. Estimated hopping conduction c) barrier height and d) hopping distance as a function of material thickness.

dependence of cross-plane transport should not be affected. However, to explain the thermally activated behavior, the extraordinary temperature sensitivity of the conduction mechanism and the anomalous behavior distinguishing the two material systems, one requires a deeper understanding of the underlying mechanisms.

To explore the material properties involved in the cross-plane conduction of NbSe<sub>2</sub> and HfS<sub>2</sub>, we now focus on the thermal response of the material and its effect on the vdWg. Raman spectroscopy is a powerful tool for probing of the anharmonicities in the chemical bonds. The barrier between the individual layers is defined by the physical and electronic properties of the vdWg. The temperature-dependent bond characteristics of HfS<sub>2</sub> and NbSe<sub>2</sub> can provide us with important information on their structural and electrical properties. We performed temperature-dependent Raman measurements on samples of vastly different thicknesses. The Raman spectra acquired at several temperatures for thin samples of NbSe<sub>2</sub> (4.8 nm thick) and HfS<sub>2</sub> (7.0 nm thick) are shown in Figure 6a,c. For NbSe<sub>2</sub>, both the E<sub>2g</sub><sup>1</sup> and the A<sub>1g</sub> peaks show a redshift to lower wavenumbers with increasing temperature (Figure 6a). Similar behavior can be seen for the E<sub>g</sub> peak of HfS<sub>2</sub> (Figure 6b). However, an opposite trend is observed for the A<sub>1g</sub> Raman mode of HfS<sub>2</sub> (Figure 6c). As the temperature increases, a gradual blueshift to higher wavenumbers is clearly visible. This behavior is qualitatively similar for thicker samples where the long-range screening and coulombic effects slightly change the response of the bonds. To understand these phenomena, we plot the changes in peak position as a function of the temperature for all of the discernable Raman active modes of both compounds (Figure 6d–g).

We quantitatively examine the temperature dependence of the Raman modes by estimating the first-order temperature coefficient,  $\chi$ , and the absolute zero vibrational frequency fit,  $\omega_0$ , via a linear fit (the results are summarized in Figure S4, Supporting Information). Changes in the Raman frequencies, expressed in the form of the first-order temperature coefficient, depend on anharmonic terms in the lattice potential energy of the materials.<sup>[21]</sup> The rate of change in the Raman frequency is dependent on the temperature effects due to anharmonic coupling of phonons, three and four phonon processes, and the

volumetric thermal expansion contributions of the crystal. The results indicate that a distinctive behavior dictates the anharmonicities in the two materials. This distinctive behavior explains the differences in magnitude and in the direction of change in the vibrational modes. The planar modes in NbSe<sub>2</sub> have a larger response to temperature. These values are much larger than those measured for HfS<sub>2</sub> and those previously extracted for MoS<sub>2</sub> considered as the standard TMD<sup>[22]</sup> (Figure S4). This can be attributed to the nature of the metallic bonds and the isotropic forces governing the interactions between the metal–ligand constituents of the NbSe<sub>2</sub> molecular structure. More importantly, a clear distinction between the out-of-plane vibrational modes of the two materials becomes evident. While NbSe<sub>2</sub> has an ordinary response to temperature and shows a redshift in the A<sub>1g</sub> mode as the temperature is increased, the out-of-plane vibrations of HfS<sub>2</sub> show the opposite behavior. In the temperature ranges where both vibrational modes, i.e., planar and out-of-plane, were examined, the most prominent contribution to the temperature dependence of the peak position should arise from volumetric effects. The rate of change in the Raman frequencies is then related to the rate of change in the stiffness of the bonds. The observation of the molecular bond response to changes in temperature unveils a distinct thermal expansion difference between the two materials. From the response of the A<sub>1g</sub> mode in HfS<sub>2</sub> samples, we conclude that as the temperature increases, one observes a net stiffening of the bonds along the cross-plane which results in a negative coefficient of thermal expansion. The bonds in NbSe<sub>2</sub> show a regular response and soften as the temperature is increased, resulting in a positive coefficient of thermal expansion.

As temperature increases, a softening of the NbSe<sub>2</sub> molecular bonds results in the thermal expansion of the layers. While vdW forces between the TMD layers are weak, they are affected by changes in temperature and should also expand in the cross-plane direction. As a result, the physical and electronic properties of the vdWgs, i.e., barrier properties, such as the effective width, heights, and hopping distances, in our tunneling models should also change. These observations suggest that the temperature dependence of the vdWg properties and the contrasting behavior observed should be partly responsible for the transport behavior in NbSe<sub>2</sub> and HfS<sub>2</sub> devices.

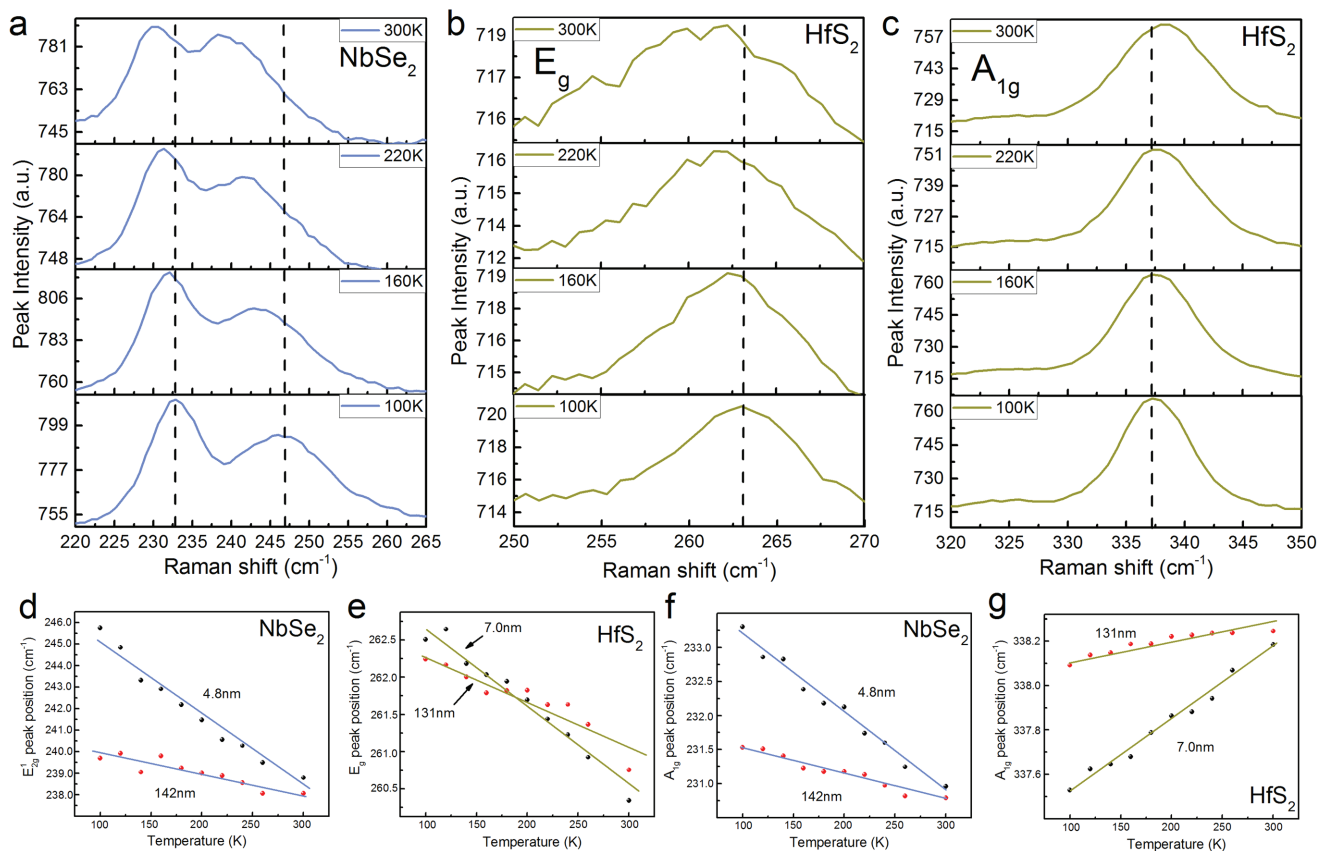


**Figure 6.** Temperature-dependent Raman spectroscopy. a) Temperature dependence of the E<sub>2g</sub> and A<sub>1g</sub> Raman modes in NbSe<sub>2</sub>. Temperature dependence of the b) E<sub>g</sub> and c) A<sub>1g</sub> modes in HfS<sub>2</sub>. Temperature dependence of Raman peak positions for the d) NbSe<sub>2</sub> E<sub>2g</sub> mode, e) HfS<sub>2</sub> E<sub>g</sub> mode, f) NbSe<sub>2</sub> A<sub>1g</sub> mode, and g) HfS<sub>2</sub> A<sub>1g</sub> modes based on sample thickness.

To provide a complete picture of the cross-plane transport in our material systems, we analyze and explain our results (Figure 2) based on the tunneling models developed here in conjunction with the thermal expansion effects on the properties of vdWgs. As the thickness is increased, the number of barriers and the density of states increase in the materials. In NbSe<sub>2</sub> where the barrier height is insignificant, this results in an increase in conductivity ( $J$ - $V$  based on relationship (3)) (Figure 2a). However, the increase in number of the barriers in HfS<sub>2</sub> shows a reverse trend as the barrier heights dictate transport in this material (Figure 2a). The nonlinear character of the thickness dependence in both materials can partially be related to the role of direct tunneling at low channel length regimes that quickly vanish at higher thicknesses ( $J$ - $V$  based on relationship (1)). Meanwhile, as the temperature increases, the enhancement of the trap-based tunneling leads to an increase in the conductivity of both materials (Figure 2b,c). For HfS<sub>2</sub>, the sensitivity to temperature is more appreciable and is higher at thicker samples due to an increase in the number of vdWgs and activity of the thermal mechanisms. For thick NbSe<sub>2</sub> (thicknesses > 10 nm) samples, however, the role of the thermal expansion on the gaps becomes a significant factor. The increase in temperature enhances the thermal mechanisms of tunneling and increases the current densities, while the gradual modification of the barrier properties, as a result of thermal expansion, progressively impedes these effects. This

results in the observed anomalous behavior in the NbSe<sub>2</sub> cross-plane transport above  $\approx 120$  K that we attribute to the vdWg thermal effects (Figure 3a). In contrast, the gradual stiffening of the bonds in the cross-plane orientation of the HfS<sub>2</sub> crystals, as the temperature rises, and the resultant negative coefficient of thermal expansion result in the contraction of the vdWgs. This combination of changes in the vdWg properties and the rise in the thermally mediated tunneling currents result in a uniform and strong surge in current densities and in the extraordinarily high thermal response in the cross-plane HfS<sub>2</sub> conduction.

### 3. Conclusion

We examined the cross-plane carrier transport properties of layered materials by studying the mechanisms of carrier tunneling in NbSe<sub>2</sub> and HfS<sub>2</sub>. The distinct properties of the two materials allowed us to broadly probe the mechanism of transport in this crystal orientation. From the temperature-dependent measurements, we conclude that the magnitude and quality of van der Waals gaps and the distinct nature of the electronic structures in the cross-plane orientation of layered materials play a central role in the carrier transport properties. The thickness-dependent transport properties in these compounds are partly correlated with the anisotropic nature of the band dispersions calculated using first principles calculations. However,

to further understand the transport results, we utilized a material model that examined the layered structure and the van der Waals characteristics of the TMDs. Using this model, we examined the van der Waals gap barrier and localized state properties of NbSe<sub>2</sub> and HfS<sub>2</sub>. The barrier model focused on thermally mediated trap-based tunneling and hopping conduction as the predominant mechanisms of transport. We determined that the thermal expansion properties of the materials along the cross-plane orientation contribute to the modification of the van der Waals gap between layers, and combined with the dominance of different tunneling mechanisms at different temperature regimes explain the electronic transport along the cross-plane crystal orientation. These results explain and support the origins of the extraordinary high temperature coefficients in HfS<sub>2</sub> and the anomalous conductivity behavior in NbSe<sub>2</sub>. Our results suggest that a focus on design of the van der Waals gap properties in cross-plane electronics will be useful in the development of material schemes for unique electronic applications.

## 4. Experimental Section

**Material Preparation:** HfS<sub>2</sub> and NbSe<sub>2</sub> samples were grown using chemical vapor transport where iodine was used as the transport agent. Hf (99.8%) and S (99.999%) were mixed stoichiometrically and sealed in a quartz ampoule under vacuum, heated up to 750 °C at a rate of 100 °C h<sup>-1</sup>, and subsequently cooled to room temperature at a rate of 10 °C h<sup>-1</sup>. The obtained material was then combined with iodine (99.999%, 1.5 mg cm<sup>-3</sup>) and heated up to a temperature of 1050 °C at a rate of 50 °C h<sup>-1</sup> with a temperature gradient of ≈50 °C and held there for 5 d, then cooled to 750 °C at a rate of 5 °C h<sup>-1</sup> and subsequently quenched to room temperature. To produce the NbSe<sub>2</sub> samples, a similar procedure was used by substituting Hf with Nb (99.8%) and S with Se (99%).

**X-Ray Photoemission Spectroscopy:** X-ray photoelectron spectroscopy was performed using a PHI 5000 VersaProbe III instrument with a monochromatic Al K $\alpha$  source. HfS<sub>2</sub> and NbSe<sub>2</sub> were exfoliated onto SiO<sub>2</sub>/Si substrates with gold marker layers, similar to those substrates used for device fabrication and testing. Two to three areas with thick exfoliated layers, identified prior to instrument loading, were scanned at an X-ray voltage of 100 kV. For each area, a survey scan was performed from 0 to 1100 eV with a pass energy of 140 eV, followed by a high-resolution scan (pass = 26.0 eV, step size = 0.05 eV) of the individual elements detected in the survey scan. MultiPak software was used to identify and fit the elemental peaks, where the spectra was shifted based on the adventitious carbon peak at a binding energy of 284.8 eV.

**Raman Spectroscopy:** Raman measurements were performed with a WITec Alpha 300RA system using the 532 nm line of a frequency-doubled neodymium-doped yttrium aluminium garnet (Nd:YAG) laser as the excitation source. The spectra were measured in the backscattering configuration using a 63 $\times$  objective and an 1800 grooves mm<sup>-1</sup> grating. The laser power was set at 250  $\mu$ W. The spot size of the laser was roughly 1  $\mu$ m resulting in an incident laser power density of ≈2.5 mW  $\mu$ m<sup>-2</sup>. This laser power was chosen to avoid causing any damage to the materials. The temperature-dependent measurements were performed in a SuperVarioTemp Janis Research cryostat adapted for Raman spectroscopy with a continuous flow of liquid nitrogen as the cooling agent. The measurements were performed under high vacuum conditions with pressures ranging between 7.5  $\times$  10<sup>-6</sup> and 1.5  $\times$  10<sup>-6</sup> Torr. The temperature-based measurements were carried out after allowing the sample and chamber temperature to stabilize for 20 min once each temperature was reached.

**Device Fabrication:** A Vistec EBPG5000+ES electron beam lithography (EBL) system was utilized with automated alignment capability for fabrication of the devices including steps for the marker layer, bottom electrode, SiO<sub>2</sub> etch, and top electrode preparation. For most of the

lithography steps, MicroChem A4 495 poly(methyl methacrylate) (PMMA) was used as the resist. Spinning the resist at a speed of 3000 rpm resulted in an ≈200 nm thick PMMA film. After defining the marker layer and bottom electrodes patterns on a 1 cm  $\times$  1 cm SiO<sub>2</sub>/Si wafer (1  $\mu$ m/500  $\mu$ m thick) using EBL, the PMMA with methyl isobutyl ketone/isopropyl alcohol (MIBK/IPA) (1:2 ratio) was developed for 90 s. This development recipe was used for all of the other steps. The metallization of Au was carried by a CHA e-Beam Vacuum Evaporator System at a mid-10<sup>-6</sup> Torr pressure range. The NbSe<sub>2</sub> and HfS<sub>2</sub> samples were then exfoliated onto the bottom electrodes. After identifying samples that were located on the bottom electrodes with optical microscopy, a second EBL step was performed to deposit electrode pads on top of the exfoliated materials. The entire substrate was then coated with a PECVD-grown SiO<sub>2</sub>. A Plasma Therm 790+ oxide/nitride PECVD system was used at 300 °C to deposit 100 nm of SiO<sub>2</sub>. A third EBL step was performed to pattern access holes to the top of the pad electrode. In this step, MicroChem A9 950PMMA with a thickness of 1400 nm (spin-coated at 300 rpm) was used. An Oxford Plasmalab 100 with a cooled substrate electrode (set at 18 °C) was used to perform the etching step. An etch recipe based on a SF<sub>6</sub>/H<sub>2</sub> (20 sccm/20 sccm) plasma at 50 W reactive-ion etching (RIE) and 1400 W inductively coupled plasma (ICP) power was calibrated and used. The etch rate calibration was performed on 0.1–1  $\mu$ m diameter test patterns. A Veeco Nanoman atomic force microscope (AFM) was used for thickness measurements of the exfoliated samples as well as the etch rate measurements. The device fabrication was finalized by patterning the top electrodes in a fourth EBL step and metallization.

**Electrical Measurements:** All of the electrical measurements were obtained using a Keithley 4200 parameter analyzer. The measurements were taken from 77 to 300 K at a pressure no greater than 2  $\times$  10<sup>-6</sup> Torr in a Lakeshore probe station with cryo capabilities. The measurements at each temperature were done after allowing for at least 20 min of hold time for the sample and chamber temperature to stabilize.

**Band Structure Calculations:** To correlate the cross-plane transport to the fundamental electronic properties, electronic properties of bulk HfS<sub>2</sub> and NbSe<sub>2</sub> DFT with the projector augmented wave method<sup>[9]</sup> were calculated as implemented in the Vienna Ab-initio Simulation package (VASP<sup>[10]</sup>) code. The structure optimization, total energy, and electronic structure calculations were performed using the generalized gradient approximation parameterized by Perdew, Burke, and Ernzerhof (PBE).<sup>[11]</sup> A plane-wave basis kinetic energy cutoff of 300 eV was used and tested to reach convergence for the lattice properties for both the systems. A  $\Gamma$ -centered Monkhorst–Pack BZ integration scheme was adopted to integrate over the BZ.<sup>[12]</sup> The lattice parameters were optimized using a coarse (6  $\times$  6  $\times$  6) k-point grid. The semiempirical DFT-D3 dispersion correction of Grimme was implemented to include the vdW interactions in the Kohn–Sham energies.<sup>[13]</sup> The forces were calculated using the Hellmann–Feynman procedure and geometries were optimized using a conjugated gradient scheme. The atomic coordinates were optimized in all directions with a convergence criterion of 0.001 eV  $\text{Å}^{-1}$  for the atomic forces. The optimized bulk lattice parameters were  $a = b = 3.6433 \text{ \AA}$ ,  $c = 6.5844 \text{ \AA}$  and  $a = b = 3.4894 \text{ \AA}$ ,  $c = 13.7569 \text{ \AA}$  for HfS<sub>2</sub> and NbSe<sub>2</sub>, respectively, which are comparable to the experimental values. Using the optimized lattice parameters, self-consistent charge calculations were performed using a denser k-grid (12  $\times$  12  $\times$  12). The calculated self-consistent charges were then used to calculate the band structure and the density of states. In order to rectify the limitations of the PBE method in underestimating the energy gap for the semiconducting HfS<sub>2</sub>, a hybrid functional (HSE06) was employed as implemented in the VASP code. The quantitative value of the vacuum level required for the work function calculation was identified by integrating the electrostatic potential on a real space grid along the cross-plane axis.

## Supporting Information

Supporting Information is available from the Wiley Online Library or from the author.

## Acknowledgements

L.B. acknowledges the U.S. Army Research Office MURI Grant W911NF-11-1-0362.

## Conflict of Interest

The authors declare no conflict of interest.

## Keywords

cross-plane electron transport, layered materials, transition metal dichalcogenides, tunneling, van der Waals gaps

Received: November 1, 2017

Revised: January 25, 2018

Published online:

- 
- [1] a) K. S. Novoselov, A. K. Geim, S. V. Morozov, D. Jiang, Y. Zhang, S. V. Dubonos, I. V. Grigorieva, A. A. Firsov, *Science* **2004**, 306, 666; b) B. Radisavljevic, A. Radenovic, J. Brivio, V. Giacometti, A. Kis, *Nat. Nanotechnol.* **2011**, 6, 147.
- [2] a) W. Primak, *Phys. Rev.* **1956**, 103, 544; b) W. Primak, L. H. Fuchs, *Phys. Rev.* **1954**, 95, 22; c) K. Kawamura, Y. Ouchi, H. Oshima, T. Tsuzuku, *J. Phys. Soc. Jpn.* **1979**, 46, 587; d) K. Matsubara, K. Sugihara, T. Tsuzuku, *Phys. Rev. B* **1990**, 41, 969.
- [3] a) L.-N. Nguyen, Y.-W. Lan, J.-H. Chen, T.-R. Chang, Y.-L. Zhong, H.-T. Jeng, L.-J. Li, C.-D. Chen, *Nano Lett.* **2014**, 14, 2381; b) G.-H. Lee, S. Kim, S.-H. Jhi, H.-J. Lee, *Nat. Commun.* **2015**, 6, 6181; c) O. I. Joshua, A. S. Gary, S. J. v. d. Z. Herre, C.-G. Andres, *2D Mater.* **2016**, 3, 031002.
- [4] T. Enoki, N. Sakamoto, K. Nakazawa, K. Suzuki, K. Sugihara, K. Kobayashi, *Phys. Rev. B* **1993**, 47, 10662.
- [5] a) L.-D. Zhao, S.-H. Lo, Y. Zhang, H. Sun, G. Tan, C. Uher, C. Wolverton, V. P. Dravid, M. G. Kanatzidis, *Nature* **2014**, 508, 373; b) R. Fei, A. Faghaninia, R. Soklaski, J.-A. Yan, C. Lo, L. Yang, *Nano Lett.* **2014**, 14, 6393; c) R. Fei, L. Yang, *Nano Lett.* **2014**, 14, 2884; d) D. Sarkar, X. Xie, W. Liu, W. Cao, J. Kang, Y. Gong, S. Kraemer, P. M. Ajayan, K. Banerjee, *Nature* **2015**, 526, 91.
- [6] a) A. D. Yoffe, *Annu. Rev. Mater. Sci.* **1973**, 3, 147; b) A. R. Beal, H. P. Hughes, W. Y. Liang, *J. Phys. C: Solid State Phys.* **1975**, 8, 4236; c) D. W. Bullett, *J. Phys. C: Solid State Phys.* **1978**, 11, 4501.
- [7] K. Terashima, I. Imai, *Solid State Commun.* **1987**, 63, 315.
- [8] R. Dhall, M. R. Neupane, D. Wickramaratne, M. Mecklenburg, Z. Li, C. Moore, R. K. Lake, S. Cronin, *Adv. Mater.* **2015**, 27, 1573.
- [9] a) C. Lee, H. Yan, L. E. Brus, T. F. Heinz, J. Hone, S. Ryu, *ACS Nano* **2010**, 4, 2695; b) K. F. Mak, C. Lee, J. Hone, J. Shan, T. F. Heinz, *Phys. Rev. Lett.* **2010**, 105, 136805.
- [10] S. I. Uchida, S. Tanaka, *J. Phys. Soc. Jpn.* **1978**, 45, 153.
- [11] J. C. Tsang, J. E. Smith, M. W. Shafer, *Phys. Rev. Lett.* **1976**, 37, 1407.
- [12] C. S. Wang, J. M. Chen, *Solid State Commun.* **1974**, 14, 1145.
- [13] a) T. Iwasaki, N. Kuroda, Y. Nishina, *J. Phys. Soc. Jpn.* **1982**, 51, 2233; b) A. Cingolani, M. Lugará, G. Scamarcio, F. Lévy, *Solid State Commun.* **1987**, 62, 121.
- [14] S. Ahmed, P. A. Lee, *J. Phys. D: Appl. Phys.* **1973**, 6, 593.
- [15] Y.-S. Kim, M. Marsman, G. Kresse, F. Tran, P. Blaha, *Phys. Rev. B* **2010**, 82, 205212.
- [16] a) G. Hautier, A. Miglio, G. Ceder, G. M. Rignanese, X. Gonze, *Nat. Commun.* **2013**, 4, 2292; b) G. Hautier, A. Miglio, D. Waroquiers, G.-M. Rignanese, X. Gonze, *Chem. Mater.* **2014**, 26, 5447.
- [17] S. K. Saha, U. V. Waghmare, H. R. Krishnamurthy, A. K. Sood, *Phys. Rev. B* **2008**, 78, 165421.
- [18] a) R. Tsu, L. Esaki, *Appl. Phys. Lett.* **1973**, 22, 562; b) L. L. Chang, L. Esaki, R. Tsu, *Appl. Phys. Lett.* **1974**, 24, 593.
- [19] a) J. G. Simmons, *J. Appl. Phys.* **1964**, 35, 2655; b) S. M. Sze, K. K. Ng, in *Physics of Semiconductor Devices*, John Wiley & Sons, Inc., Hoboken, NJ **2006**, p. 415; c) F.-C. Chiu, *Adv. Mater. Sci. Eng.* **2014**, 2014, 18.
- [20] a) W. Zhou, X. Zou, S. Najmaei, Z. Liu, Y. Shi, J. Kong, J. Lou, P. M. Ajayan, B. I. Yakobson, J.-C. Idrobo, *Nano Lett.* **2013**, 13, 2615; b) S. Najmaei, Z. Liu, W. Zhou, X. Zou, G. Shi, S. Lei, B. I. Yakobson, J.-C. Idrobo, P. M. Ajayan, J. Lou, *Nat. Mater.* **2013**, 12, 754.
- [21] a) E. S. Zouboulis, M. Grimsditch, *Phys. Rev. B* **1991**, 43, 12490; b) R. A. Cowley, *Adv. Phys.* **1963**, 12, 421; c) P. G. Klemens, *Phys. Rev.* **1966**, 148, 845; d) C. Postmus, J. R. Ferraro, S. S. Mitra, *Phys. Rev.* **1968**, 174, 983.
- [22] a) S. Najmaei, P. M. Ajayan, J. Lou, *Nanoscale* **2013**, 5, 9758; b) N. A. Lanzillo, A. G. Birdwell, M. Amani, F. J. Crowne, P. B. Shah, S. Najmaei, Z. Liu, P. M. Ajayan, J. Lou, M. Dubey, S. K. Nayak, T. P. O'Regan, *Appl. Phys. Lett.* **2013**, 103, 093102.